Germanium substitution endowing Cr^{3+}-doped Zinc aluminate phosphors with bright and super-long near-infrared persistent luminescence

Yi Zhang[a] ,Rui Huang[a*], Hongliang Li[a], Dejian Hou[a], Zhenxu Lin[a], Jie Song[a], Yuzheng Guo[b*], Huihong Lin[a], Chao Song[a], Zewen Lin[c], and John Robertson[d]

Corresponding authors: Rui Huang: rhuang@hstc.edu.cn; Yuzheng Guo: yuzheng.guo@swansea.ac.uk

[a]School of Materials Science and Engineering, Hanshan Normal University, Chaozhou, Guangdong 521041, China

[b]College of Engineering, Swansea University, Swansea, SA1 8EN, United Kingdom

[c]School of Electronic Science and Engineering, Nanjing University, Nanjing, Jiangsu 210093, China

[d]Department of Engineering, University of Cambridge, Cambridge CB2 1PZ, United Kingdom

Abstract: We present novel near-infrared (NIR) Cr^{3+}-doped non-gallate super-long-persistence phosphors ($Zn_{1+x}Al_{2-2x}Ge_xO_4:Cr^{3+}$) by Germanium substitution in the original $ZnAl_2O_4:Cr^{3+}$. Unlike the negligible NIR persistent luminescence of $ZnAl_2O_4:Cr^{3+}$ upon UV or visible light excitation, the Ge substituted phosphors feature strong and super-long-persistent luminescence at approximately 650–750 nm for more than 120 h. The relation between the Ge substitution and the defect trapping states is investigated systematically. The experimental results combined with the first-principles calculations reveal that $Ge_{Zn}^{\circ\circ}$ and Ge_{Al}° in the spinel structure would introduce shallow and deep defect states in the band gap to serve as new efficient traps, which are mainly responsible for the strong and super-long-persistent luminescence upon UV or visible light excitation. The present advanced phosphors is an alternative candidate for applications in biomedical imaging and night-vision surveillance.

Keywords: Persistent luminescence, Near-infrared, First-principles, Antisite

defects, Energy storage

1. Introduction

Persistent phosphors, which continuously emit for minutes to hours after termination of the excitation source, have long attracted great interest because of their wide applications, such as in security signs, traffic signs, and emergency route signs. Currently, several long-persistent phosphors (LPPs), such as $CaAl_2O_4:Eu^{2+}$, Nd^{3+} (blue emission, >5 h) [1], $SrAl_2O_4:Eu^{2+}$, Dy^{3+} (green emission, >30 h) [2], and $Y_2O_2S:Eu^{3+}$, Mg^{2+}, Ti^{4+} (red emission, >5 h) [3], have been commercialized as night-vision materials for various important innovations. In recent years, near-infrared (NIR) LPPs for biomedical imaging applications have been extensively developed [4–9]. The NIR LPPs not only feature light emission in the optical bioimaging window but also enable bioimaging without external excitation [4,10,11]. Thus, NIR LPPs used as optical bioimaging probes can increase the penetration depth in tissues and avoid the autofluorescence of body tissues under continuous illumination [12]. These characteristics significantly improve the signal-to-noise ratio (S/N) and sensitivity. Given the similar ionic radii of Cr^{3+} and Ga^{3+} ions and the suitable host crystal field strength around Cr^{3+}, Cr^{3+}-doped gallate materials have been systematically studied to obtain enhanced NIR emission and duration [13–17]. Among these materials, $Zn_3Ga_2Ge_2O_{10}:Cr^{3+}$ phosphors have been found to possess super-long NIR persistent luminescence durations of more than 360 h [18]. Moreover, NIR persistent luminescence can be excited by natural sunlight

in almost all types of outdoor environments. In addition to Cr^{3+}-doped gallate materials, Cr^{3+}-doped non-gallate materials with NIR persistent luminescence have also been developed. Li et al. reported that $Zn_{2-x}Al_{2x}Sn_{1-x}O_4:Cr^{3+}$ phosphors feature an emission band ranging from 650 nm to 1200 nm with NIR persistent luminescence lasting over 35 h [19]. More recently, Liang et al. reported that $MgGeO_3:Yb^{3+}$ phosphors exhibit persistent shortwave IR luminescence at approximately 1000 nm with a long persistence time of more than 100 h [20].

For LPPs, the defect trapping states, including the trap distribution and density, which are generally associated with lattice defects, are the most important factors that determine the intensity and duration of persistent luminescence [21–24]. To obtain the desired persistent luminescence performance, conduction band (CB) engineering and/or co-dopants are usually used to adjust the trap distribution and/or density [24,25]. These strategies have been demonstrated in studies on $Zn_{1+x}Ga_{2-2x}Ge_xO_4:Cr^{3+}$, $Zn_{2-x}Al_{2x}Sn_{1-x}O_4:Cr^{3+}$ and $Zn_xGa_2O_{3+x}:Cr^{3+}$ [17,19,26,27]. Extensive studies have also been performed to provide new insights on the defect trapping states. The performance of NIR persistent luminescence in Cr^{3+}-doped phosphors was found to strongly depend on the local environment of Cr ions [28,29]. For Cr^{3+}-doped AB_2O_4 spinel compounds, shallower defects located far from Cr^{3+} ions are responsible for the persistent luminescence induced by band excitation, while persistent luminescence induced by visible light excitation is determined

by the local environment of Cr^{3+} ions [30]. NIR persistent luminescence from $ZnGa_2O_4$ induced by visible light excitation results from Cr^{3+} ions with an anti-site defect in their first cationic neighbor [28,29,31,32]. Priolkar et al. showed that a small degree of inversion disorder is also necessary for visible light to produce persistent luminescence [29]. Although great progress has been made, tailoring NIR persistent materials for specific applications still remains a challenge. In particular, the defect trapping states that determining the persistent luminescence performance still remains unclear.

$ZnAl_2O_4$ is an AB_2O_4 compound with a spinel structure [33]. $ZnAl_2O_4$ comprises two types of coordination polyhedra with the octahedral sites occupied by Al^{3+} ions and the tetrahedral sites occupied by Zn^{2+} ions, similar to the structure of $ZnGa_2O_4$. Cr^{3+}-emitter centers easily substitute for Al^{3+} ions to yield NIR emission because of the similar ionic radii of Cr^{3+} (0.755 Å, for coordination number (CN) = 6) and Al^{3+} (0.675 Å, for CN = 6). However, $ZnAl_2O_4$:Cr^{3+} features very feeble NIR persistent luminescence upon UV or visible light excitation, and this negligible persistent luminescence is attributed to the small inversion disorder (less than 1%) in $ZnAl_2O_4$ [29].

In this work, a series of novel non-gallate $Zn_{1+x}Al_{2-2x}Ge_xO_4$:Cr^{3+} NIR LPPs were fabricated for the first time. The $Zn_{1.2}Al_{1.6}Ge_{0.2}O_4$:$Cr^{3+}$ phosphors exhibit strong and super-long-persistent luminescence at approximately 650–750 nm for more than 120 h. The NIR persistent luminescence can be triggered by UV and visible light. The relation between the Ge substitution and the defect

trapping states is investigated. The remarkable improvement of the presented LPPs is discussed.

2. Experimental

2.1 Materials and Preparation Method.

$Zn_{1+x}Al_{2-2x}Ge_xO_4$:0.5%Cr^{3+} (x = 0–0.4) phosphors were synthesized through high-temperature solid-state sintering. Samples were denoted ZAO, ZAGO1, ZAGO2, ZAGO3, and ZAGO4, where x = 0, 0.1, 0.2, 0.3, and 0.4, respectively. Pure ZnO (4N), Al_2O_3 (4N), GeO_2 (4N), and Cr_2O_3 (4N) were used as raw materials. The powders were finely mixed in an agate mortar to form homogeneous powders for prefiring. After prefiring at 1000 °C for 2 h, the materials were ground again to fine powders. All phosphors were sintered at 1400 °C for 6 h.

2.2 Characterization.

Phase purity was confirmed by the X-ray diffraction (XRD) patterns recorded with a D8 Advance Bruker Bragg-Brentano diffractometer (Cu Kα radiation) equipped with a Vantec-1 linear detector. Photoluminescence (PL) spectra were measured at 77 K using a LabRAM HR Evolution micro-Raman spectrometer equipped with a CCD detector. The samples were mounted on a thermal stage with a second harmonic 532 nm Nd-YAG laser for excitation. PL spectra, PL excitation (PLE) spectra, persistent luminescence emission (PersL) spectra, persistent luminescence excitation (PersLE) spectra, and persistent luminescence decay curves were recorded at room temperature using a

Fluorolog-3 spectrofluorometer equipped with a photomultiplier. A 450 W xenon lamp was chosen as the excitation source. Diffuse reflectance spectra of the samples were recorded using a scanning spectrophotometer with a $BaSO_4$-based integrating sphere. The thermoluminescence (TL) curves were recorded using the spectrofluorometer and a setup consisting of a copper sample holder and a compact furnace with programmable heating and double-gratings (1200 gr/mm, 500 nm blaze) in the emission monochromator with a CCD camera. For the TL measurement, a sample was heated at a linear heating rate of 2 K/s. All digital photographs were taken using a camera phone (Meizu, Metal).

2.3 Computational and details and modeling.

The band structure of $Zn_{1+x}Al_{2-2x}Ge_xO_4$:0.5%Cr^{3+} was calculated with the planewave pseudopotential code CASTEP [34]. The screened exchange hybrid functional was used to obtain an accurate band structure [35]. The same parameters as those in our previous work on transition metal oxides were used [36,37]. To characterize the doping effects, a supercell of 56 atoms was used for all the calculations. A 3×3×3 MP grid was used for k-point sampling when calculating the density of states (DOS). We have found that Cr forms an antiferromagnetic order, so spin-polarization was used for all the calculations. A larger 2×1×1 supercell was used for odd-number defects, such as Al_{Zn}°, to eliminate the single spin interaction

3. **Results and Discussion**

Fig. 1 shows the emission and excitation spectra of the $ZnAl_2O_4$:Cr^{3+} (ZAO)

and $Zn_{1.2}Al_{1.6}Ge_{0.2}O_4:Cr^{3+}$ (ZAGO2) samples at room temperature. Under excitation at 387 nm, both samples exhibit the same emission lines resulting from the $^2E \rightarrow {}^4A_2$ spin-forbidden transition of Cr^{3+} in an octahedral crystal field [18]. The zero-phonon R lines located at 686.0 nm are associated with the Cr^{3+} in unperturbed octahedral sites [29,32]. The R lines are accompanied by their Stokes phonon side bands (PSB), which ranged from 707 to 717 nm, and anti-Stokes PSB, which ranged from 666 to 678 nm. The N2 lines at 694.3 nm correspond to Cr^{3+} ions with a neighboring antisite defect [29,32]. The most important feature of these two spectra is that the emission band from ZAGO2 become broader than the emission band from ZAO. This phenomenon may have resulted from the increasing disorder of the Cr^{3+} ions in the host material induced by the incorporation of Ge. The PLE spectra at 686 nm emission cover a very broad spectral region and consist of three main excitation bands. The bands at approximately 530 nm (band 1) and 385 nm (band 2) correspond to the $^4A_2 \rightarrow {}^4T_2$ and $^4A_2 \rightarrow {}^4T_1$ (^4F) transitions of Cr^{3+} ions. The band (band 3) between 280 nm and 320 nm is ascribed to the electronic transition from $^4A_2$ to the CB of the host [10,18]. Band 3 obviously shifts to lower energy with an increase in x (Fig. S1 Supporting Information). This phenomenon is consistent with the reduction in the optical band gap with increasing x (Fig. S2) [17]. The low-energy side of bands 1 and 2 slightly redshifts with increasing x. This shift can be attributed to the weakening of the crystal field with increasing x (Table S1 and Fig. S3) [19].

Interestingly, after removal of the excitation source, strong and super-long-persistent NIR luminescence can be observed from the Ge-substituted samples. Fig. 2 shows the change in the brightness of NIR persistent luminescence with the decay time and the decay curve of the persistent luminescence for the ZAGO2 discs monitored at 690 nm after irradiation by a 280 nm xenon lamp for 15 min. The persistent luminescence intensity decreases quickly in the first 30 min and then decays slowly. The intensity of the NIR persistent luminescence is very strong such that it can be clearly observed with the naked eye and easily imaged by a normal camera phone even after 30 min of decay, as shown in Fig. 2 (b). After 120 h of decay, the intensity of the persistent emission remains significantly high. This result indicates that the NIR persistent luminescence should last much longer than 120 h. This behavior is completely different from that observed for ZAO, where no persistent luminescence can be found after 280 nm excitation.

PersLE spectra were examined to determine the effective excitation wavelength region for persistent luminescence. The PersLE spectrum of ZAGO2 monitored at 690 nm is shown in Fig. 3, which is acquired using different excitation wavelengths between 260 nm to 650 nm in 10 nm steps. The PersLE spectrum exhibits an intense band ranging from 260 nm to 340 nm that corresponds to the transition from $^4A_2$ to the CB. This result demonstrates that the NIR persistent luminescence from ZAGO2 can be effectively triggered by 260–340 nm excitation, which is considered to occur because of the

assistance by the host CB. A weak PersLE band ranging from 450 nm to 550 nm, which is associated with the $^4A_2 \rightarrow {}^4T_2$ transition, can also be detected for ZAGO2. This implies that visible light from the blue region to the yellow region can still charge the phosphor and induce persistent NIR emission. This weak PersLE band becomes more intense and extends to 610 nm in ZAGO3. Thus, the persistent luminescence can be more efficiently excited with visible light from the blue region to the orange–red region after appropriately increasing the Ge concentration in phosphor. It is noticed that no persistent luminescence can be found from phosphors at x = 0 UV and Vis as the excitation light. This result implies that the incorporation of Ge plays an important role in the production of persistent luminescence.

Fig. 4 (a) presented XRD patterns of $Zn_{1+x}Al_{2-2x}Ge_xO_4:Cr^{3+}$ (x = 0–0.4) samples. All diffraction peaks of the samples are in agreement with those of ICSD No. 75098, and no impurity can be detected. Increasing the value of x results in the gradual deviation of the diffraction peaks from the standard peaks and the movement of these peaks to lower 2θ side [38,39]. It's probably ascribed from the lattice expansion induced by the replacement of Zn^{2+} (r = 0.88 Å, CN (coordination number) = 6) for Al^{3+} (r = 0.675 Å, CN = 6) in the octahedral sites. Considering the close ionic radius of Ge^{4+} (r = 0.67 Å, CN = 6) and Al^{3+}, Al^{3+} in the octahedral sites are presumably substituted by Ge^{4+}. Besides, there is a possibility that Ge^{4+} enter into the tetrahedral sites. The classical spinel structure that comprises two types of coordination polyhedra with octahedral

and tetrahedral sites is also shown in Fig. 4 (b). Thus, this non-equivalent substitution probably creates positive octahedral defects (Ge_{Al}°), negative octahedral defects ($Zn_{Al}^{'}$) and positive tetrahedral defects ($Ge_{Zn}^{\circ\circ}$) in the spinel structure [19,26]. The antisite defects may act as effective traps, contributing to the strong and super-long-persistent luminescence.

To gain more insight into the effects of the antisite defects, the band structure of a typical supercell and various antisite defects states are calculated with the screened exchange hybrid functional. The typical Cr-doped supercell, which is based on the spinel structure of $ZnAl_2O_4$ with Ge and Cr taking six-fold sites, is shown in Fig. S5 (a). The DOS of the perfect cell in Fig. 5 shows a clear band gap of 4.3 eV, which is close to the measured value of 4.1 eV based on the Kubelka-Munk transformed diffuse reflectance spectra shown in Fig. S2 [40]. The CB minimum is mainly composed of d electrons from Ge/Zn and p electrons from O. The increase in the Ge concentration shifts the CB edge down and thus narrows the band gap, which is in good agreement with the experimental results shown in Fig. S2. The different antisite defects were further analyzed in Fig. 5, and the corresponding atomic structures are given in Fig. S5. $Zn_{Al}^{'}$ and Al_{Zn}° antisite defects can introduce deep levels in the mid-gap region. The Ge_{Al}° antisite defect introduces shallow defect states just 0.5 eV below the CB. Interestingly, the $Ge_{Zn}^{\circ\circ}$ antisite defect can produce defect states spanning from the mid-gap region to the CB edges.

To further elucidate the role of Ge substitution in the trap properties, TL

spectra of $Zn_{1+x}Al_{2-2x}Ge_xO_4:Cr^{3+}$ are examined. Figs. 6 (a) and (b) show TL glow curves of the Cr^{3+} emission from the ZAGO2 phosphors. Under irradiation by high-energy light (280 nm), a broad TL peak, which reflects the trap depth, is located at 405 K. With an increase in decay time, the TL peak position gradually moves toward the high-temperature region. This phenomenon indicates that the detrapping process gradually shifts from the shallow traps to the deep traps over the decay time. Moreover, the TL peak intensity, which reflects the concentration of charge carriers stored in the traps, becomes gradually weaker. The TL band peak at 445 K remains obvious after 120 h of decay, implying that a considerable number of charge carriers remain stored in the deep traps even after 120 h of natural decay. The charge carriers released from the deep traps contribute to the super-long-persistent luminescence shown in Fig. 2 (a). Based on the spectral shape of the TL band, the trap depth energies were estimated using an initial rising analysis method [22]. This approach assumes that the concentration of trapped electrons on the low-temperature side of a TL glow curve is relatively constant. Thus, the TL intensity can be written as:

$$I(T) = C \times \exp\left(\frac{-E}{kT}\right)$$

where *I* is the TL intensity, *T* is the temperature, *k* is Boltzmann constant, and *C* is the fitting constant. Therefore, by plotting the TL curve as ln (T) versus 1/T, the trap depth can be estimated from the slope of the straight fitting line on the low-temperature side. When the decay time increases from 10 min to 120 h, the trap depth energy gradually increases from ~0.57 to ~1.50 eV (Fig. S6),

and this increase verifies the presence of a continuous and wide trap depth distribution in ZAGO2. Moreover, as the irradiation shifts toward low-energy light, the low-temperature band of the TL peak gradually disappears, and the high-temperature band still exists. Consequently, the TL peak shifts to 445 K after irradiation at 540 nm, and this behavior is identical to that of the TL peak after 120 h of decay. This result implies that visible-light irradiation is unable to activate shallow traps but promotes the filling of deep traps. Notably, under irradiation at 540 nm, the active energy that enables the $^4A_2 \rightarrow {}^4T_2$ transition is much lower than the active energy that enables the $^4A_2 \rightarrow$CB transition. This result indicates that electron trapping and detrapping recombination processes in the deep traps of ZAGO2 do not occur through band assistance but rather through energy-matched tunneling channels. This tunneling process proceeds slowly, resulting in the super-long-persistent luminescence at room temperature.

Figs. 6 (c) and (d) further show TL spectra of $Zn_{1+x}Al_{2-2x}Ge_xO_4:Cr^{3+}$ with different x values. Under irradiation at 280 nm, the dominant TL peak shifts to the lower temperature region as x increases from 0.1 to 0.4, indicating that the trap depth becomes shallower. The trap depth estimated by an initial rising approach gradually decreases from 0.73 eV to 0.36 eV (Fig. S7 (a)), which exhibits the same variation as that of the optical band gap with x, as shown in Fig. 7. This phenomenon suggests that the reduction in the trap depth is a result of the decrease in band gap. This process is referred to as band gap engineering [41]. However, ZAGO2 presents the most intense persistent

luminescence among all samples upon 280 nm excitation, as shown in Fig. S4 (a). The reduction in trap depth does not increase the persistent luminescence intensity. These results imply that band gap engineering is not the key factor determining the persistent luminescence intensity and duration in our case. Under irradiation at 540 nm, the intensity of the dominant TL peak increases with x and reaches a maximal value at x = 0.3. This result indicates that the moderate incorporation of Ge can effectively increase the concentration of the deep traps that can be filled from the energy-matched Cr^{3+} energy levels via tunneling. According to these TL results, the deep trap depth estimated by an initial rising approach (Fig. S7 (b)) slightly decreases from 1.25 eV to 1.21 eV with increasing x, as shown in Fig. 7.

Apparently, the trap depth distribution estimated by TL spectra coincides well with the distribution of $Ge_{Zn}^{\circ\circ}$ and Ge_{Al}° antisite defect states obtained by the first-principles calculations. Therefore, the $Ge_{Zn}^{\circ\circ}$ and Ge_{Al}° antisite defects are considered to serve as the main electron trapping centers responsible for the strong and super-long persistent luminescence. Under UV (260-340 nm) excitation, the ground-state electrons of Cr^{3+} ions are photoionized to the CB. These electrons are subsequently captured by the traps induced by the $Ge_{Zn}^{\circ\circ}$ and Ge_{Al}° antisite defects. The captured electrons in shallow traps escape thermally through the CB and recombine with the ionized Cr^{3+} ions to generate initial intense NIR persistent luminescence [31]. On the other hand, the captured electrons in deep traps can be released through energy-matched

tunneling channels because of the wide trap distribution indicated in Fig. 5 [18]. This tunneling process proceeds slowly, yielding weak but super-long persistent NIR luminescence. Under visible light (400-610 nm) irradiation, the electrons are photoionized to the low-energy excited states and tunnel across a short distance to the nearby energy-matched deep traps. The captured electrons undergo reverse tunneling upon thermal disturbance at room temperature and directly recombine with the ionized Cr^{3+} ions, followed by NIR persistent luminescence. Therefore, it is very easy to understand how visible light can still activate the presented phosphor to produce NIR persistent luminescence even though the energy of visible light is below the ionization threshold.

To further understand the persistent luminescence mechanism induced by visible light excitation, low-temperature PL measurements are performed. Fig. 8 (a) shows the PL spectra of $Zn_{1+x}Al_{2-2x}Ge_xO_4:Cr^{3+}$ (x = 0–0.4) samples at 77 K under excitation by a 532 nm laser. The zero-photon R1 and R2 lines, corresponding to Cr^{3+} ions in unperturbed octahedral sites (referred as Cr_R ions), are observed at 686.2 nm and 685.2 nm, respectively [28,29]. The N1 lines at 689.2 nm may be assigned to Cr^{3+} ions close to $Ge_{Zn}^{\circ\circ}$ antisite defects (Cr_{N1} ions), whereas the N2 lines at 694.3 nm are presumably attributed to the presence of $Zn_{Al}^{'}$ and Ge_{Al}° antisite defects close to the Cr^{3+} ions as the first cationic neighbor (Cr_{N2} ions) [29]. The low-temperature PL spectrum of $Zn_{1+x}Al_{2-2x}Ge_xO_4:Cr^{3+}$ (x = 0) shows an intense R line with negligible N1 and N2 lines. With an increase in x, the N1 and N2 lines become stronger and wider. This

phenomenon strongly indicates that the incorporation of Ge causes the non-equivalent substitution and thus significantly increases the antisite defects related to Cr_{N1} and Cr_{N2} ($Ge_{Zn}^{\circ\circ}$, Ge_{Al}° and $Zn_{Al}^{'}$). This non-equivalent substitution would inevitably enhance the inversion disorder of the host material [26,29,32]. This is further confirmed by the fact that the as-measured N1/R1 and N2/R1 line intensity ratios remarkably increase with x, as shown in Fig. 8 (b). The evolution of the inversion disorder with x also exhibits a tendency similar to that of the persistent luminescence intensity with x under 540 nm excitation (Fig. S4 (b)), indicating that the increasing disorder induced by the substitution mechanism could contribute to the remarkable improvement in the persistent luminescence properties induced by 540 nm excitation [26]. This assertion is supported by Priolkar et al., who stated that a small degree of inversion disorder is favorable for the enhancement of the persistent luminescence induced by visible-light excitation [29]. Persistent luminescence would deteriorate with increasing x over 0.3 upon 540 nm excitation. This phenomenon could be due to the self-recombination of the excited states between neighboring defects [25].

4. Conclusion

We developed efficient NIR Cr^{3+}-doped non-gallate phosphors ($Zn_{1+x}Al_{2-2x}Ge_xO_4:Cr^{3+}$, x = 0-0.4) using high-temperature solid-state sintering. The substitution of Ge enables the $Zn_{1+x}Al_{2-2x}Ge_xO_4:Cr^{3+}$ phosphors to possess bright and super-long-persistent NIR luminescence for more than 120 h. This luminescence can be triggered by UV and visible light (280–610 nm). The Ge^{4+}

non-equivalent substitution is demonstrated to produce $Ge_{Zn}^{\circ\circ}$ and Ge_{Al}° in the spinel structure, which introduces shallow and deep defect states in the band gap to serve as new efficient traps, being mainly responsible for the strong and super-long-persistent luminescence upon UV or visible light excitation. The present results demonstrate that $Zn_{1+x}Al_{2-2x}Ge_xO_4:Cr^{3+}$ phosphors can be very competitive candidate materials for use in biomedical imaging and night-vision surveillance.

Acknowledgments

This work was supported by National Natural Science Foundation of China (Nos. 61274140 and 61306003), Natural Science Foundation of Guangdong Province (2015A030313871), the Distinguished Young Teacher Training Program in Higher Education of Guangdong (YQ2015112) and Young Talents in Higher Education of Guangdong, China 2017.

References

[1] T. Katsumata, T. Nabae, K. Sasajima, T. Matsuzawa, Growth and characteristics of long persistent $SrAl_2O_4$-and $CaAl_2O_4$-based phosphor crystals by a floating zone technique, J. Cryst. Growth. 183 (1998) 361–365.

[2] T. Matsuzawa, A New Long Phosphorescent Phosphor with High Brightness, $SrAl_2O_4:Eu^{2+},Dy^{3+}$, J. Electrochem. Soc. 143 (1996) 2670.

[3] J. Hölsä, T. Laamanen, M. Lastusaari, M. Malkamäki, J. Niittykoski, E. Zych, Effect of Mg^{2+} and Ti^{IV} doping on the luminescence of $Y_2O_2S:Eu^{3+}$, Opt. Mater. 31 (2009) 1791–1793.

[4] Z. Li, Y. Zhang, X. Wu, L. Huang, D. Li, W. Fan, G. Han, Direct Aqueous-Phase Synthesis of Sub-10 nm “Luminous Pearls” with Enhanced *in Vivo* Renewable Near-Infrared Persistent Luminescence, J. Am. Chem. Soc. 137

(2015) 5304–5307.

[5] J.-L. Li, J.-P. Shi, C.-C. Wang, P. Li, Y. Zhen-feng, H.-W. Zhang, Five-Nanometer $ZnSn_2O_4$:Cr,Eu Ultra-Small Nanoparticles as New Near Infrared-Emitting Persistent Luminescent Nanoprobes for Cellular and Deep Tissue Imaging at 800 nm, Nanoscale. (2017).

[6] A. Abdukayum, J.-T. Chen, Q. Zhao, X.-P. Yan, Functional Near Infrared-Emitting Cr^{3+}/Pr^{3+} Co-Doped Zinc Gallogermanate Persistent Luminescent Nanoparticles with Superlong Afterglow for *in Vivo* Targeted Bioimaging, J. Am. Chem. Soc. 135 (2013) 14125–14133.

[7] T. Maldiney, B.-T. Doan, D. Alloyeau, M. Bessodes, D. Scherman, C. Richard, Gadolinium-Doped Persistent Nanophosphors as Versatile Tool for Multimodal In Vivo Imaging, Adv. Funct. Mater. 25 (2015) 331–338.

[8] R. Zou, J. Huang, J. Shi, L. Huang, X. Zhang, K.-L. Wong, H. Zhang, D. Jin, J. Wang, Q. Su, Silica shell-assisted synthetic route for mono-disperse persistent nanophosphors with enhanced in vivo recharged near-infrared persistent luminescence, Nano Res. 10 (2017) 2070–2082.

[9] Z. Li, Y. Zhang, X. Wu, X. Wu, R. Maudgal, H. Zhang, G. Han, In Vivo Repeatedly Charging Near-Infrared-Emitting Mesoporous $SiO_2/ZnGa_2O_4:Cr^{3+}$ Persistent Luminescence Nanocomposites, Adv. Sci. 2 (2015) 1500001.

[10] T. Maldiney, A. Bessière, J. Seguin, E. Teston, S.K. Sharma, B. Viana, A.J.J. Bos, P. Dorenbos, M. Bessodes, D. Gourier, D. Scherman, C. Richard, The in vivo activation of persistent nanophosphors for optical imaging of vascularization, tumours and grafted cells, Nat. Mater. 13 (2014) 418–426.

[11] S.K. Singh, Red and near infrared persistent luminescence nano-probes for bioimaging and targeting applications, RSC Adv. 4 (2014) 58674–58698.

[12] Z. Xue, X. Li, Y. Li, M. Jiang, H. Liu, S. Zeng, J. Hao, X-ray-Activated Near-Infrared Persistent Luminescent Probe for Deep-Tissue and Renewable in Vivo Bioimaging, ACS Appl. Mater. Interfaces. 9 (2017) 22132–22142.

[13] A. Bessière, S. Jacquart, K. Priolkar, A. Lecointre, B. Viana, D. Gourier, $ZnGa_2O_4:Cr^{3+}$: a new red long-lasting phosphor with high brightness, Opt.

Express 19 (2011) 10131-10137.
[14] D. Chen, Y. Chen, H. Lu, Z. Ji, A Bifunctional Cr/Yb/Tm:$Ca_3Ga_2Ge_3O_{12}$ Phosphor with Near-Infrared Long-Lasting Phosphorescence and Upconversion Luminescence, Inorg. Chem. 53 (2014) 8638–8645.
[15] Y. Jin, Y. Hu, L. Yuan, L. Chen, H. Wu, G. Ju, H. Duan, Z. Mu, Multifunctional near-infrared emitting Cr^{3+}-doped $Mg_4Ga_8Ge_2O_{20}$ particles with long persistent and photostimulated persistent luminescence, and photochromic properties, J Mater Chem C. 4 (2016) 6614–6625.
[16] F. Liu, W. Yan, Y.-J. Chuang, Z. Zhen, J. Xie, Z. Pan, Photostimulated near-infrared persistent luminescence as a new optical read-out from Cr^{3+}-doped $LiGa_5O_8$, Sci. Rep. 3 (2013).
[17] Y. Zhuang, J. Ueda, S. Tanabe, P. Dorenbos, Band-gap variation and a self-redox effect induced by compositional deviation in $Zn_xGa_2O_{3+x}$:Cr^{3+} persistent phosphors, J. Mater. Chem. C. 2 (2014) 5502.
[18] Z. Pan, Y.-Y. Lu, F. Liu, Sunlight-activated long-persistent luminescence in the near-infrared from Cr3+-doped zinc gallogermanates, Nat. Mater. 11 (2011) 58–63.
[19] Y. Li, Y. Li, R. Chen, K. Sharafudeen, S. Zhou, M. Gecevicius, H. Wang, G. Dong, Y. Wu, X. Qin, J. Qiu, Tailoring of the trap distribution and crystal field in Cr^{3+}-doped non-gallate phosphors with near-infrared long-persistence phosphorescence, NPG Asia Mater. 7 (2015) e180.
[20] Y.-J. Liang, F. Liu, Y.-F. Chen, X.-J. Wang, K.-N. Sun, Z. Pan, New function of the Yb^{3+} ion as an efficient emitter of persistent luminescence in the short-wave infrared, Light Sci. Appl. 5 (2016) e16124–e16124.
[21] A. De Vos, K. Lejaeghere, D.E.P. Vanpoucke, J.J. Joos, P.F. Smet, K. Hemelsoet, First-Principles Study of Antisite Defect Configurations in $ZnGa_2O_4$:Cr Persistent Phosphors, Inorg. Chem. 55 (2016) 2402–2412.
[22] K. Van den Eeckhout, A.J.J. Bos, D. Poelman, P.F. Smet, Revealing trap depth distributions in persistent phosphors, Phys. Rev. B. 87 (2013).
[23] J. Botterman, J.J. Joos, P.F. Smet, Trapping and detrapping in $SrAl_2O_4$: Eu,

Dy persistent phosphors: Influence of excitation wavelength and temperature, Phys. Rev. B. 90 (2014).

[24] T. Maldiney, A. Lecointre, B. Viana, A. Bessière, M. Bessodes, D. Gourier, C. Richard, D. Scherman, Controlling Electron Trap Depth To Enhance Optical Properties of Persistent Luminescence Nanoparticles for In Vivo Imaging, J. Am. Chem. Soc. 133 (2011) 11810–11815.

[25] Y. Li, Y.-Y. Li, K. Sharafudeen, G.-P. Dong, S.-F. Zhou, Z.-J. Ma, M.-Y. Peng, J.-R. Qiu, A strategy for developing near infrared long-persistent phosphors: taking $MAlO_3$:Mn^{4+}, Ge^{4+} (M = La, Gd) as an example, J. Mater. Chem. C. 2 (2014) 2019.

[26] M. Allix, S. Chenu, E. Véron, T. Poumeyrol, E.A. Kouadri-Boudjelthia, S. Alahrache, F. Porcher, D. Massiot, F. Fayon, Considerable improvement of long-persistent luminescence in germanium and tin substituted $ZnGa_2O_4$, Chem. Mater. 25 (2013) 1600–1606.

[27] Y. Li, S. Zhou, Y. Li, K. Sharafudeen, Z. Ma, G. Dong, M. Peng, J. Qiu, Long persistent and photo-stimulated luminescence in Cr^{3+}-doped Zn–Ga–Sn–O phosphors for deep and reproducible tissue imaging, J. Mater. Chem. C. 2 (2014) 2657.

[28] D. Gourier, A. Bessière, S.K. Sharma, L. Binet, B. Viana, N. Basavaraju, K.R. Priolkar, Origin of the visible light induced persistent luminescence of Cr^{3+}-doped zinc gallate, J. Phys. Chem. Solids. 75 (2014) 826–837.

[29] N. Basavaraju, K.R. Priolkar, D. Gourier, S.K. Sharma, A. Bessière, B. Viana, The importance of inversion disorder in the visible light induced persistent luminescence in Cr^{3+} doped AB_2O_4 (A = Zn or Mg and B = Ga or Al), Phys Chem Chem Phys. 17 (2015) 1790–1799.

[30] S.K. Sharma, D. Gourier, B. Viana, T. Maldiney, E. Teston, D. Scherman, C. Richard, Persistent luminescence of AB_2O_4:Cr^{3+} (A=Zn, Mg, B=Ga, Al) spinels: New biomarkers for in vivo imaging, Opt. Mater. 36 (2014) 1901–1906.

[31] A. Bessière, S.K. Sharma, N. Basavaraju, K.R. Priolkar, L. Binet, B. Viana, A.J.J. Bos, T. Maldiney, C. Richard, D. Scherman, D. Gourier, Storage of Visible

Light for Long-Lasting Phosphorescence in Chromium-Doped Zinc Gallate, Chem. Mater. 26 (2014) 1365–1373.

[32] N. Basavaraju, K.R. Priolkar, D. Gourier, A. Bessière, B. Viana, Order and disorder around Cr^{3+} in chromium doped persistent luminescent AB_2O_4 spinels, Phys Chem Chem Phys. 17 (2015) 10993–10999.

[33] S.-H. Wei, S. Zhang, First-principles study of cation distribution in eighteen closed-shell $A^{II}B_2^{III}O_4$ and $A^{IV}B_2^{II}O_4$ spinel oxides, Phys. Rev. B. 63 (2001). doi:10.1103/PhysRevB.63.045112.

[34] M.D. Segall, P.J.D. Lindan, M.J. Probert, C.J.Pickard, P.J.Hasnip, S.J lark, M.C.Payne, First-principles simulation: ideas, illustrations and the CASTEP code, J. Phys.: Condens. Matter, 14 (2002) 2717–2744.

[35] S.J. Clark, J. Robertson, Screened exchange density functional applied to solids, Phys. Rev. B. 82 (2010).

[36] S.J. Clark, J. Robertson, S. Lany, A. Zunger, Intrinsic defects in ZnO calculated by screened exchange and hybrid density functionals, Phys. Rev. B. 81 (2010).

[37] Y. Guo, S.J. Clark, J. Robertson, Electronic and magnetic properties of Ti_2O_3, Cr_2O_3 , and Fe_2O_3 calculated by the screened exchange hybrid density functional, J. Phys. Condens. Matter. 24 (2012) 325504.

[38] M. Chen, Z. Xia, M.S. Molokeev, C.C. Lin, C. Su, Y.-C. Chuang, Q. Liu, Probing Eu^{2+} Luminescence from Different Crystallographic Sites in $Ca_{10}M(PO_4)_7$:Eu $^{2+}$ (M = Li, Na, and K) with β-$Ca_3(PO_4)_2$ -Type Structure, Chem. Mater. 29 (2017) 7563–7570.

[39] M. Chen, Z. Xia, M.S. Molokeev, T. Wang, Q. Liu, Tuning of Photoluminescence and Local Structures of Substituted Cations in $x$$Sr_2Ca(PO_4)_2$–(1–$x$)$Ca_{10}Li(PO_4)_7$:Eu^{2+} Phosphors, Chem. Mater. 29 (2017) 1430–1438.

[40] V.D.-M.Ž. Barbarić-Mikočević, K. Itrić, Kubelka-Munk theory in describing optical properties of paper (I), Tech. Gaz. 18 (2011) 117–124.

[41] J. Ueda, P. Dorenbos, A.J.J. Bos, K. Kuroishi, S. Tanabe, Control of

electron transfer between Ce^{3+} and Cr^{3+} in the $Y_3Al_{5-x}Ga_xO_{12}$ host via conduction band engineering, J Mater Chem C. 3 (2015) 5642–5651.

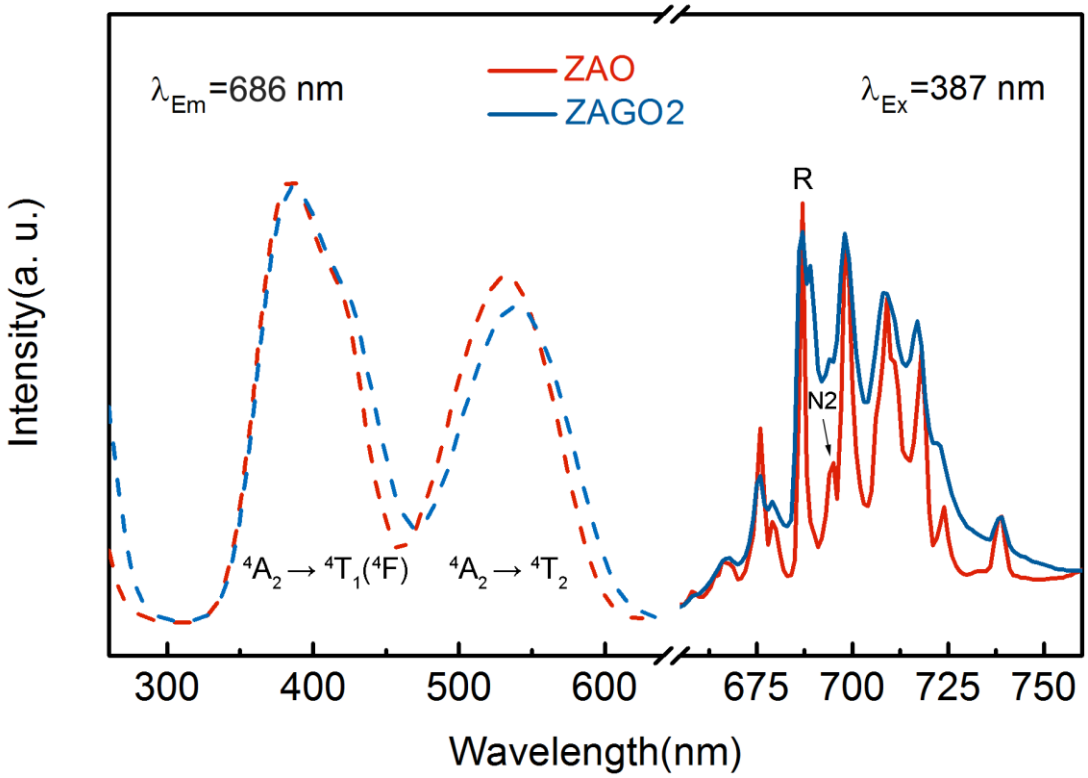

Figure 1. PL spectra of $ZnAl_2O_4:Cr^{3+}$ (ZAO) and $Zn_{1.2}Al_{1.6}Ge_{0.2}O_4:Cr^{3+}$ (ZAGO2) samples (ZAGO2) acquired under excitation at 387 nm, and PLE spectra of ZAO and ZAGO2 obtained with monitoring at 686 nm.

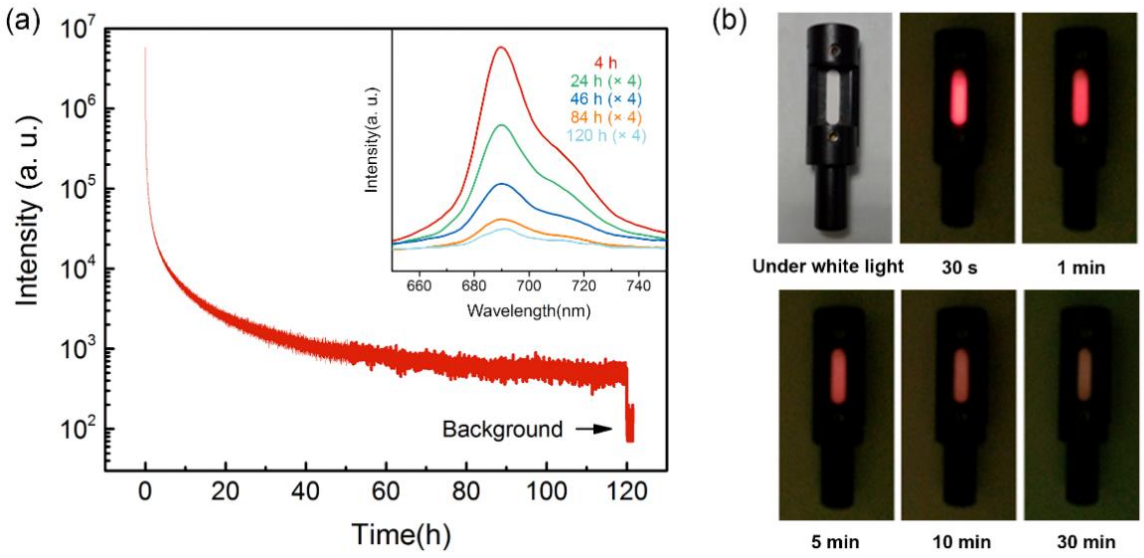

Figure 2. (a) Persistent luminescence decay curve of the $Zn_{1.2}Al_{1.6}Ge_{0.2}O_4:Cr^{3+}$ sample (ZAGO2) at 690 nm emission with a decay time of more than 120 h after irradiation by a 280 nm xenon lamp for 10 min. The inset shows the persistent luminescence spectra acquired at different decay times. The persistent emissions peak at approximately 690 nm and the profiles of the persistent luminescence spectra do not change with the decay time. (b) NIR afterglow images (photograph parameters: manual/ISO 1600/exposure time of 10 s) at different afterglow times (30 s to 30 min).

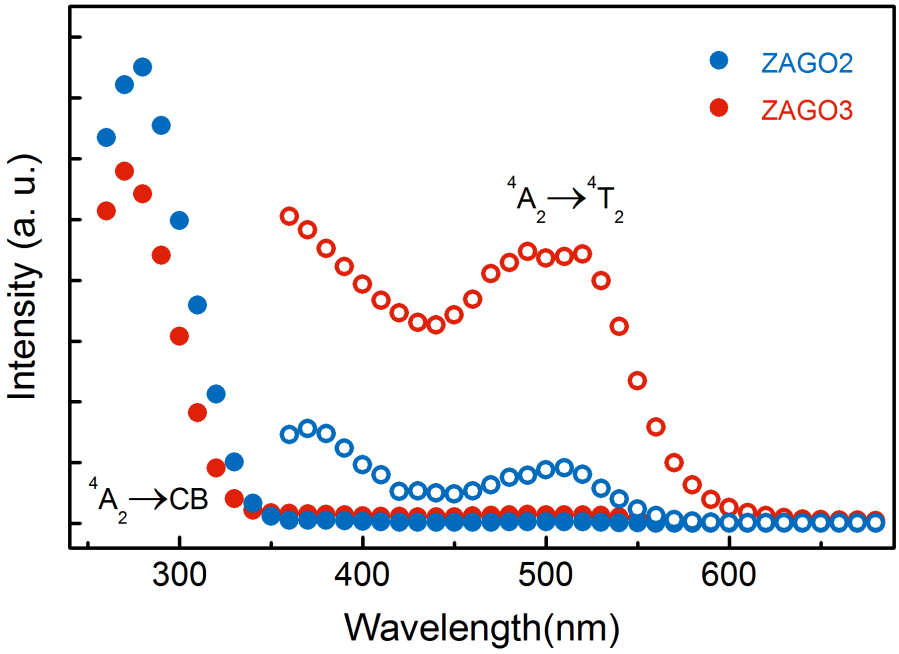

Figure 3. PersLE spectra of ZAGO2 and ZAGO3 with emission recorded at 690 nm. The solid circles represent the sum of the persistent luminescent intensity from 60 to 70 s after the stoppage of each excitation. The open circles represent the magnification (×30) of the corresponding solid circles.

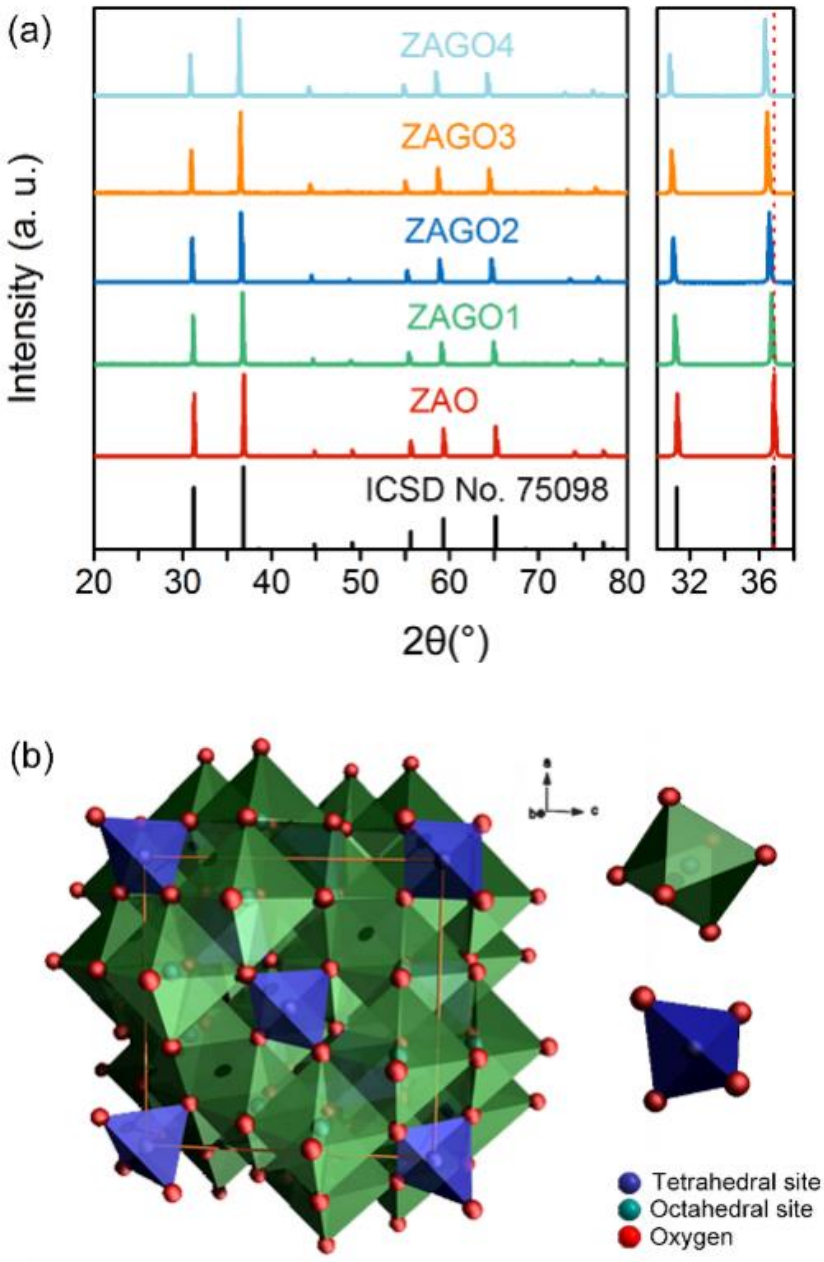

Figure 4. (a) XRD patterns of $Zn_{1+x}Al_{2-2x}Ge_xO_4:Cr^{3+}$ (x = 0−0.4) samples and the standard data for the $ZnAl_2O_4$ phase, (b) Crystal structure of normal spinel, showing octahedral and tetrahedral coordination.

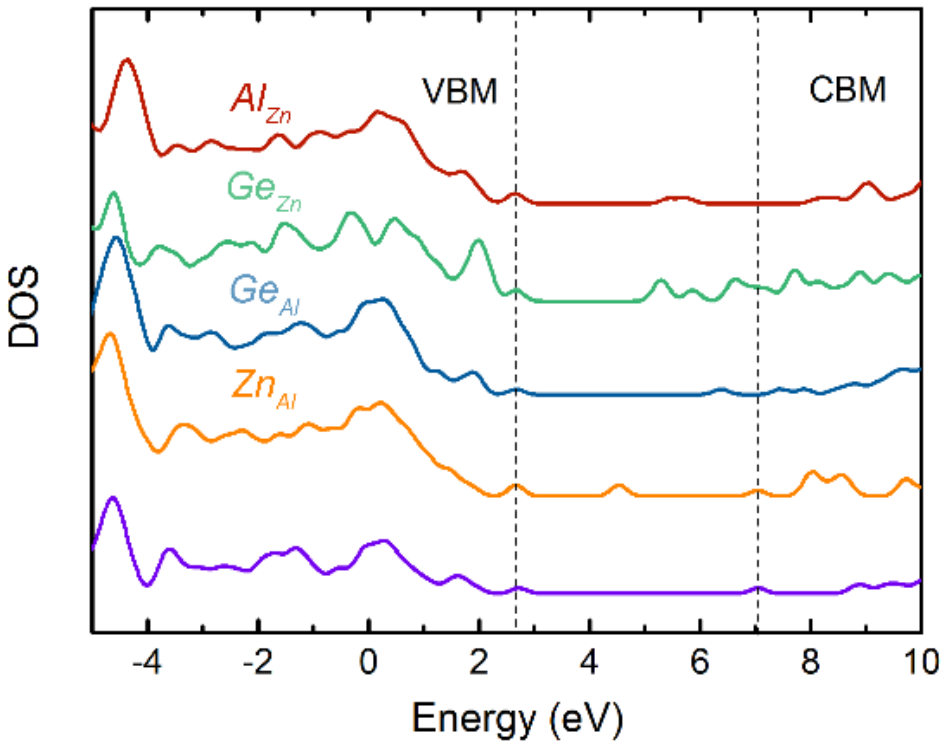

Figure 5. The partial DOS of various antisite defects: Ge_{Al}°, $Zn_{Al}^{'}$, $Ge_{Zn}^{\circ\circ}$, and Al_{Zn}°. The structure is based on the spinel structure of $ZnAl_2O_4$ with Ge and Cr taking six-fold sites. The bottom panel shows the perfect supercell without any defects, producing a band gap of 4.3 eV.

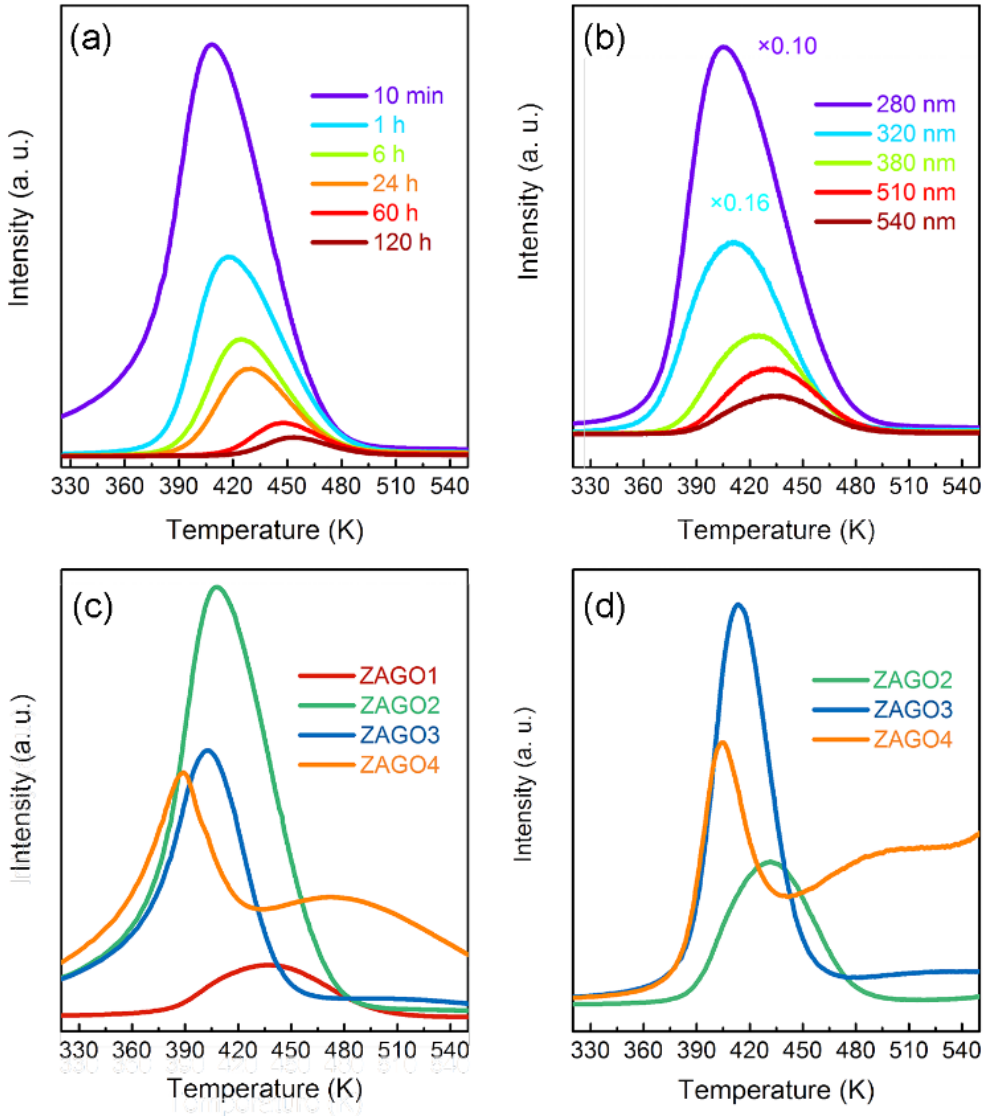

Figure 6. TL curves monitored at 690 nm emission for the $Zn_{1.2}Al_{1.6}Ge_{0.2}O_4:Cr^{3+}$ sample (ZAGO2) for a) different decay times and b) different irradiation energies. TL curves monitored at 690 nm emission for the $Zn_{1+x}Al_{2-2x}Ge_xO_4:Cr^{3+}$ samples with x varied from 0.1 to 0.4 under irradiation at different wavelengths: c) λ_{ex} = 280 nm and d) λ_{ex} = 540 nm.

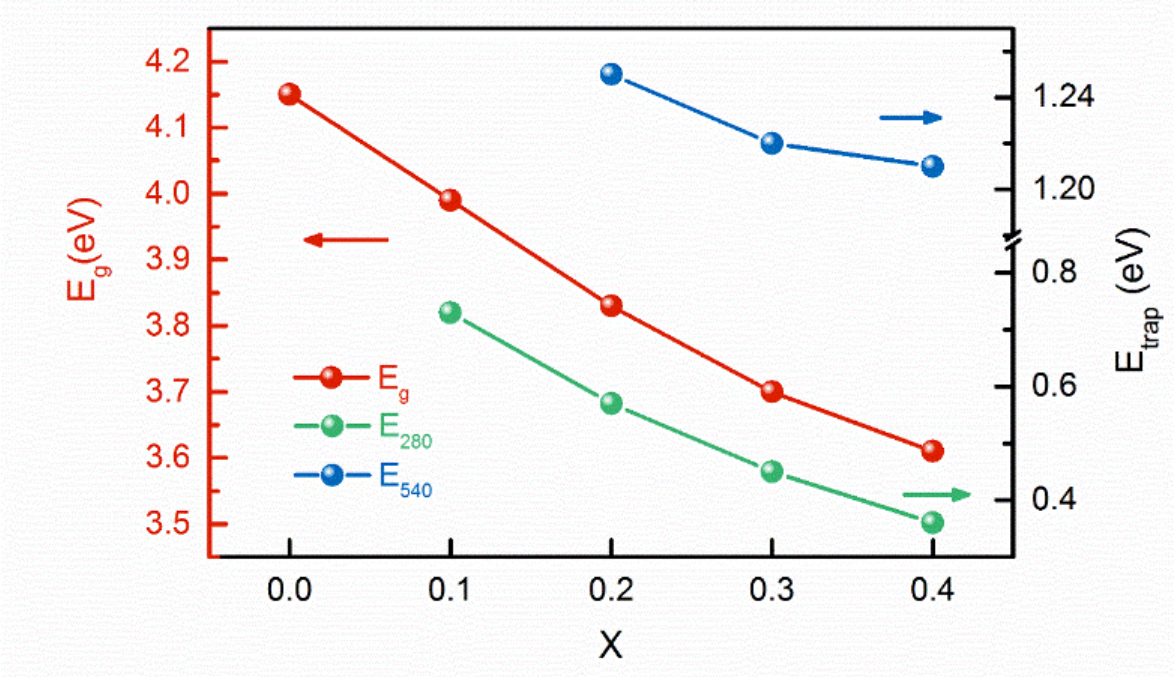

Figure 7. Trap depths estimated according to the initial rise approach and bang gap energy determined according to the Kubelka-Munk function for $Zn_{1+x}Al_{2-2x}Ge_xO_4:Cr^{3+}$ (x = 0−0.4) samples

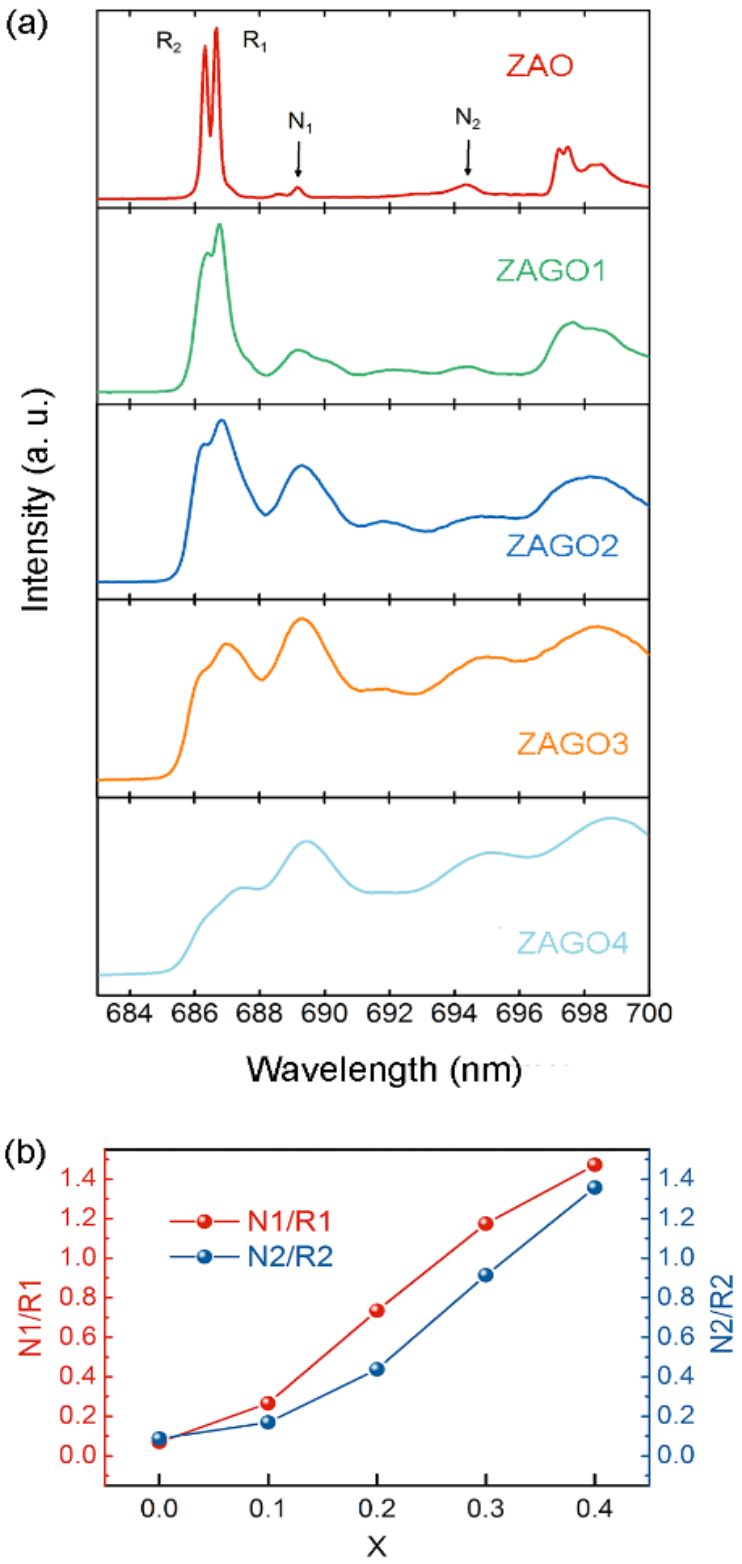

Figure 8. (a) PL spectra of the $Zn_{1+x}Al_{2-2x}Ge_xO_4:Cr^{3+}$ (x = 0−0.4) samples acquired at 77 K under excitation by a 532 nm laser, (b) Intensity ratios of the emission peaks, N1/R1 and N2/R1, as functions of x in the $Zn_{1+x}Al_{2-2x}Ge_xO_4:Cr^{3+}$ (x = 0−0.4) samples.